APPLIED SCIENCES AND ENGINEERING

The multifunctional use of an aqueous battery for a high capacity jellyfish robot

Xu Liu[1]†, Shuo Jin[2]†, Yiqi Shao[2], Sofia Kuperman[3], Autumn Pratt[1], Duhan Zhang[1], Jacqueline Lo[1], Yong Lak Joo[2], Amir D. Gat[3], Lynden A. Archer[2]*, Robert F. Shepherd[1]*

The batteries that power untethered underwater vehicles (UUVs) serve a single purpose: to provide energy to electronics and motors; the more energy required, the bigger the robot must be to accommodate space for more energy storage. By choosing batteries composed primarily of liquid media [e.g., redox flow batteries (RFBs)], the increased weight can be better distributed for improved capacity with reduced inertial moment. Here, we formed an RFB into the shape of a jellyfish, using two redox chemistries and architectures: (i) a secondary $ZnBr_2$ battery and (ii) a hybrid primary/secondary ZnI_2 battery. A UUV was able to be powered solely by RFBs with increased volumetric (Q ~ 11 ampere-hours per liter) and areal (108 milliampere-hours per square centimeter) energy density, resulting in a long operational lifetime (T ~ 1.5 hours) for UUVs composed of primarily electrochemically energy-dense liquid (~90% of the robot's weight).

INTRODUCTION

The need for more power and energy to prolong the operation time in untethered robots has always been an important goal (*1*–*4*). Enlarging the robot's size to accommodate higher capacity and more powerful energy storage systems typically comes at a cost of reduced architectural design freedom and increased inertia, reducing efficiency, agility, and increasing cost of transport (*5*–*8*).

Energy systems for present day robots are usually single purpose (*9*–*13*); to increase the operation time, the engineer must choose a higher energy density battery or add more battery volume to the robot (*2*). The high energy density of lithium-ion batteries makes them the usual choice for robots (*14*, *15*). By embodying the electrochemical energy stored in batteries into an integral part of the robot's structure and machinery, the battery can become a larger portion of the mass and volume of the robot's desired form, reducing inertial and drag effects while also increasing capacity (*16*–*20*). This scheme of embodied energy is common in nature, where most components serve multiple functions (*20*, *21*). For example, a jellyfish also uses energy multifunctionally. It is largely composed of "mesoglea" that makes its body elastic, helps restore body shape after deformation, and serves as an internal skeleton to support the body. This mesoglea is composed of fibrillin-containing microfibrils that the jellyfish uses to power its muscle and allow it to move and feed (*22*).

Previously, we demonstrated the concept of multifunctional use of liquid electrolyte from a redox flow battery (RFB) as both a hydraulic fluid and electrical energy storage in a swimming untethered underwater vehicle (UUV), shaped like a lionfish (*17*). In this UUV, the ion-selective membrane of the RFB separated the charged species stored in the catholyte (oxidized medium) and anolyte (reduced medium). The different redox potential in the electrolytes drives ion exchange through the membrane and electron movement from anolyte to catholyte through the electrodes, which powers the pumps that caused the fish to swim using hydraulic actuators. In this system, the capacity of the RFB's scale with available charge stored in the electrolyte reservoir, while the electrochemical reaction rate at the electrode stack determines the current output (*23*). Little attention, however, was paid to maximizing the capacity of the robot, or reducing its inertia by minimizing its weight or tuning its shape.

There is, therefore, an opportunity to simultaneously increase the robot's capacity with multifunctional use of RFB's, while also enhancing agility with precise design of the battery's shape. For example, if a cuboid battery design defined the shape of a robot, then its moment of inertia (I) would be unnecessarily large, limiting its ability to change direction swiftly (Fig. 1A). For increasingly large robots, this boxy shape would increase the inertial moment proportionately; in contrast, a hemispherical robot would suffer a much smaller increase in I. While a hemispherical casing could be added to envelope the cube, it would increase the total skin friction of the robot due to the increased surface area. In our liquid battery paradigm, it is easy to build a hemispherical robot geometry that is filled completely with electrolyte and, therefore, scales electrical capacity with size while easily shaping the robot for improved agility.

Here, we chose the jellyfish's shape as inspiration for increased energy storage in a simple and efficient swimming robot. The bell allows for a large proportion of liquid electrolyte storage relative to solid elements such as current collectors, and its hemispherical shape results in a relatively low moment of inertia compared to other potential geometries (Fig. 1, A and B).

We ultimately used four liters of electrolyte to fill the elastomeric bell of our Jellyfish, yielding an estimated 44-Wh capacity. To transduce this energy capacity to enough power for motor-driven swimming, we created electrolyte flow conditions and a current collector structure to yield power densities as high as P ~ 150 mW cm^{-2}. The motor, powered by the RFB, causes a network of tendons pulling on two bar linkages to drive the Jellyfish's bell up and down, to swim speeds of up to 2 cm s^{-1}. The motion of the bell causes the electrolyte to replenish ions in contact with the current collector, removing the need for dedicated pumps as is typical in RFB energy storage (Fig. 1C).

For the RFB electrolyte fluids, we chose aqueous zinc-ion–based electrolytes due to their chemical simplicity, high theoretical energy

[1]Sibley School of Mechanical and Aerospace Engineering, Cornell University, Ithaca, NY 14853, USA. [2]Robert Frederick Smith School of Chemical and Biomolecular Engineering, Cornell University, Ithaca, NY 14853, USA. [3]Faculty of Mechanical Engineering, Technion-Israel Institute of Technology, Haifa 3200003, Israel.
*Corresponding author. Email: laa25@cornell.edu (L.A.A.); rfs247@cornell.edu (R.F.S.)
†These authors contributed equally to this work.

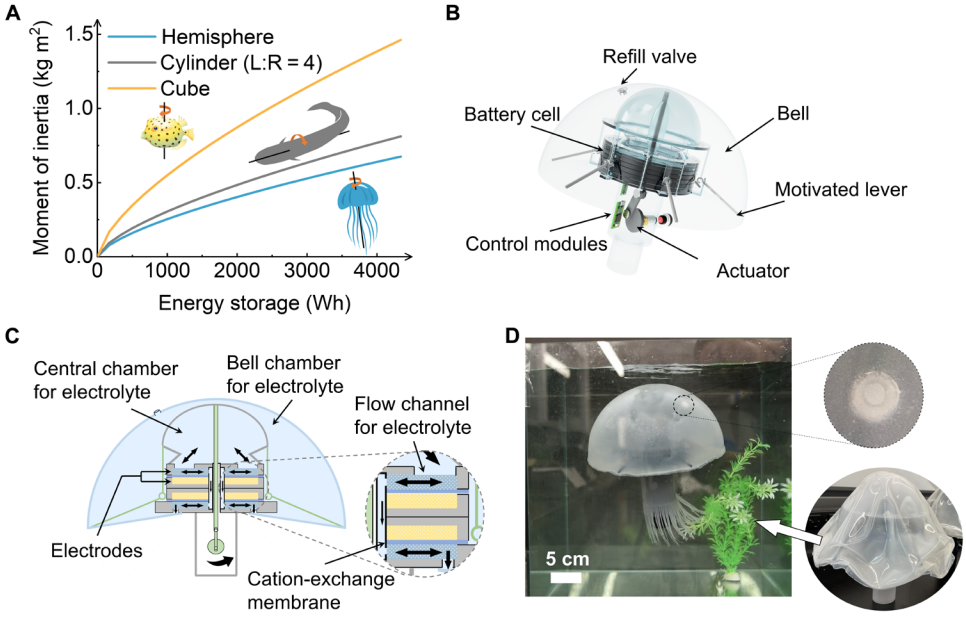

Fig. 1. A jellyfish robot powered by the RFBs. (**A**) The moment of inertia and energy storage of different geometries. (**B**) Illustration of a jellyfish robot. (**C**) Schematic of the aqueous energy systems in the jellyfish robot. (**D**) The assembled jellyfish robot powered by $ZnBr_2$ flow battery.

density ($Q \sim 1014$ A·hour liter^{-1}, 19 M for $ZnBr_2$; and $Q \sim 375$ A·hour liter^{-1}, 7 M for ZnI_2), high expected power density ($P > 100$ mW cm^{-2}), and relatively lower cost. The large volume of electrolyte used requires 3 hours to recharge; however, we have introduced a rapid recharging method to robotics that reduces the charging time to 9 min. To facilitate rapid charging, we designed our Jellyfish UUV with a valve that allows emptying of spent electrolyte with charged fluid (Fig. 1D and fig. S1).

RESULTS

Actuation system design

We used an RFB stack as the Jellyfish's power system, a motor (85 rpm, 6 V, 0.6 A, no-load, Pololu 4797) as the actuation system, and a Teensy 3.2 microcontroller (DEV 13736, SparkFun Electronics, 5 V, 30 mA) as the control system (fig. S2). The RFB converts chemical energy into electricity to power the motor and spin the crankshaft that moves the central rod up and down. This rod causes six lever arms connected, equidistantly around the inner circumference of the bell, to pivot up and down and mimic jellyfish propulsion.

Control system design

Figure 2A shows the control system of the robot. Like the actuation system, the RFB stack also powers the Teensy 3.2 microcontroller (DEV 13736, SparkFun Electronics, 5 V, 30 mA) and motor driver carrier (DRV 8838, Pololu, 0.7 W). The microcontroller and motor driver control the motor's rotation speed, thereby regulating the robot's swimming velocity. The swimming speed is not only controlled by the voltage set by Teensy but also limited by the total power density able to be provided from the flow battery. During our robot test, we set the motor duty cycle to 100% to get the highest swimming speed. We three-dimensionally (3D) printed the cylinder chamber with a diameter of 6 cm and height of 7 cm with a high modulus polyurethane (Carbon Inc.; RPU 70). Bonded together with the hollow silicone urethane (Carbon 3D Inc.; SIL 30) piece and central rod, the RPU cylinder chamber created an air space for control modules (fig. S2). The air in the control module chamber increases the robot's buoyancy, which helps to counter the slight density difference of the electrolyte ($\rho \sim 1.2$ g ml^{-1}) from the surrounding water ($\rho \sim 1$ g ml^{-1}). To maintain the Jellyfish in an upright orientation during operation, we also designed an enclosure at the bottom of the robot to add additional weights. The positioning of the central mass also allowed for controlling the robot's orientation as dictated by specific operational requirements.

Power system design

We closely tailored the RFB power system design to fit the robot (Fig. 2B). We used 3D printed polymer (Carbon Inc.; LOCTITE 3D IND405 Clear) as battery sealings to reduce the robot's total dry weight to 574 g, compared to 2207 g for the usual stainless-steel versions (Fig. 2C). We designed the overall RFB stack as a cylinder with a diameter of 12 cm. Each RFB is 0.55 cm thick, including two pieces of titanium mesh as current collectors, carbon felt electrodes, a Nafion membrane, and the 3D printed sealings. The U-shaped channels joined all anolyte (catholyte in ZnI_2 battery) chambers to allow the electrolyte to flow through all $ZnBr_2$ batteries.

When integrating the RFB into the robot system, power density governs the maximum operational speed, and areal capacity determines the overall operational duration. To achieve both high power density and capacity for the RFB, multiple fundamental challenges are known to limit the system's potential. The most important are the formation of mossy/dendritic Zn deposits that can short-circuit the cell (*24*–*26*) and the crossover issue of Br_2 or I_2 after charging (*27*, *28*). To tackle these challenges for our $ZnBr_2$ battery, we take advantage of graphene's ability as an interfacial material capable of templating Zn electrocrystalization of Zn with preferred growth axis in the plane of the current collector (*29*, *30*) and electrosprayed activated carbon to facilitate adsorption and improve electrochemical reaction kinetics at the Br_2 cathode (*31*). The graphene has crystallographic facets with

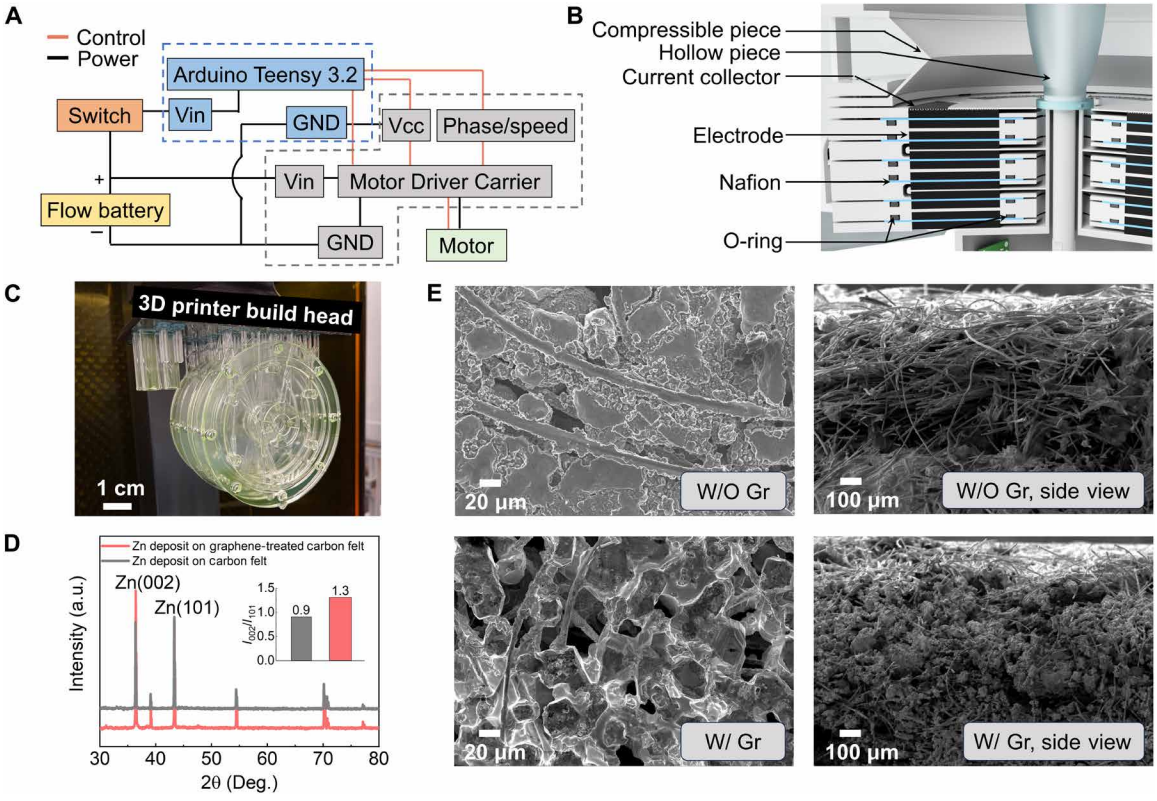

Fig. 2. The system fabrication of the Jellyfish. (**A**) Block diagram showing the control system design of the Jellyfish. (**B**) Power system design of the Jellyfish. (**C**) 3D printing of flow battery shell. (**D**) XRD test of Zn deposition on carbon felt. a.u., arbitrary units. (**E**) Scanning electron microscopy images of Zn deposition on carbon felt.

low lattice mismatch with the Zn. It shows a similar atomic arrangement to the $(0002)_{Zn}$ plane for epitaxial electrodeposition of Zn to form a coherent or semicoherent interface. It effectively drives the deposition of Zn with a locked crystallographic orientation relation. X-ray diffraction (XRD) analysis confirmed the ordered growth of zinc metal deposition on the graphene coatings (Fig. 2D). In comparison to the carbon felt without graphene (with an I_{002}/I_{101} ratio of 0.9), the extended Zn growth on the graphene-coated electrode reveals more exposure of the (002) crystal planes (with an I_{002}/I_{101} ratio of 1.3).

Furthermore, as Fig. 2E shows, Zn metal deposition occurs exclusively on the surface of the pristine carbon felt electrode without graphene treatment. This phenomenon is also confirmed by the nonuniform distribution observed in the cross-sectional scanning electron microscopy images. In contrast, the aligned graphene layers facilitated a consistent and even growth of Zn, resulting in the infiltration of Zn into the carbon felt. Moreover, the active carbon layers on the cathode side increase the effective surface area available for Br_2 adsorption and electrochemical reaction, limiting crossover (fig. S3).

$ZnBr_2$ flow battery

Here, we chose the aqueous $ZnBr_2$ RFB to power the Jellyfish system due to its high power density compared to other aqueous Zn-based RFBs (*31*). Figure 3A shows the schematic of a single $ZnBr_2$ RFB cell, while Fig. 3B provides an overview of $ZnBr_2$ RFB's integration with the Jellyfish UUV. During charge and discharge cycles, the anode reaction at both the anode and the cathode is simple: $Zn^{2+} + 2e^- \leftrightarrow Zn$ (anode) and $2Br^- - 2e^- \leftrightarrow Br_2$ (cathode), with an overall potential difference of 1.8 V. When designing the robot, to ensure operation safety and avoid the Br_2 release during operation, we sealed the catholyte and cathode carbon felt as the sessile electrode in the RFB with no flow. Consequently, our $ZnBr_2$ RFB demonstrates a stable charging and discharging plateau at a current density as high as 40 mA cm^{-2}, maintaining an average discharge voltage of ~1.6 V (Fig. 3C). Furthermore, the modified interface enhances the system's cycling stability. As illustrated in Fig. 3D, the $ZnBr_2$ RFB consistently operates at 40 mA cm^{-2} and 3.5 A·hour $liter^{-1}$ for over 40 cycles while maintaining a stable discharge plateau. Notably, the $ZnBr_2$ RFB exhibits a high power density of 146 mW cm^{-2} at 100 mA cm^{-2}, as evidenced in Fig. 3E.

To interrogate the efficiency of a $ZnBr_2$ RFB battery stack, we stacked two $ZnBr_2$ RFBs using the 3D printed battery modules (Fig. 3B) and monitored the discharge curves. As demonstrated in Fig. 3F, a stable discharge plateau in the 3.2- to 3.4-V range is seen, validating the effectiveness of the two-cell stack. In operation, the battery powered a single motor that turned a crankshaft that pulls a central rod downward, compressing a central chamber that reduces its volume and expels the electrolyte from the central chamber. On its path from the central chamber to the bell, the electrolyte enters the battery stack, filled the chambers, saturates the carbon felt, flows over the ion-selective membranes, and lastly exits the battery through the opposite end of the stack (fig. S4A). Following half a rotation cycle of the motor, the central rod ascends, decompressing the central chamber and facilitating a reverse flow of the electrolyte

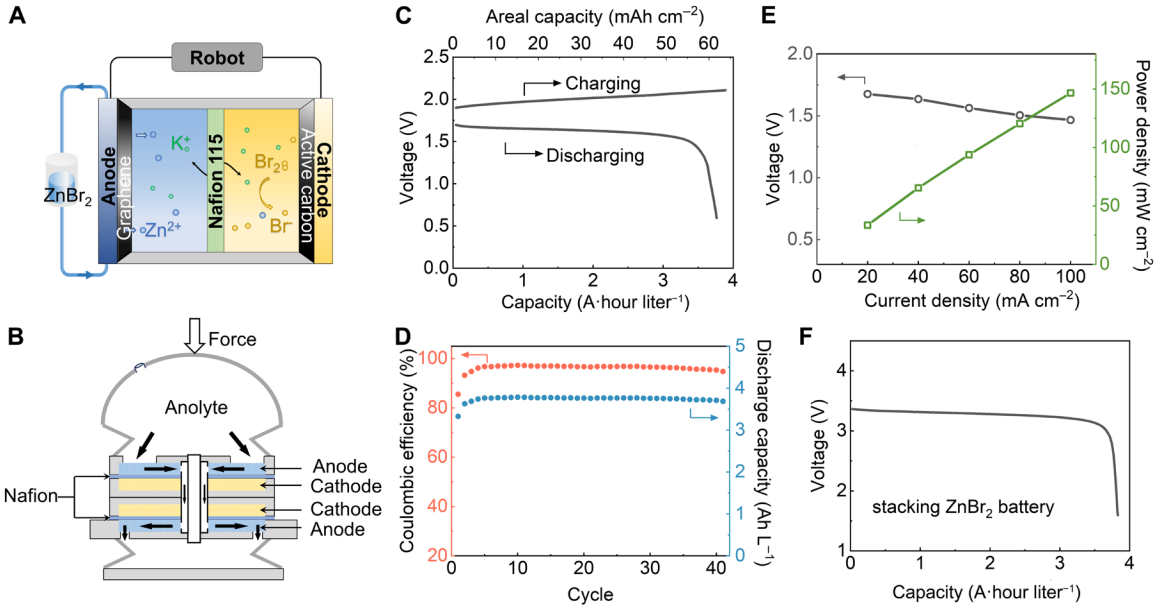

Fig. 3. $ZnBr_2$ flow battery system for high power density support of the Jellyfish. (**A**) Scheme illustrating the structure of $ZnBr_2$ RFB. (**B**) The battery stack design inside the Jellyfish. (**C**) Charge and discharge polarization curves of the single-flow battery cell with 3 M KCl + 2 M $ZnBr_2$ at a current density of 40 mA cm^{-2}. (**D**) The cycling performance of the single-flow battery cell at a current density of 40 mA cm^{-2}. (**E**) The voltage and power density of $ZnBr_2$ flow battery cells at different current densities. (**F**) Galvanostatic voltage profiles of the two stacked flow battery cells with 3 M KCl and 2 M $ZnBr_2$ at a current density of 40 mA cm^{-2}.

(fig. S4B). We achieved volume change of the central chamber by making a compressible piece using a soft 3D printed material, SIL 30, coupled with another hollow SIL 30 piece used to separate the control chamber and bell chamber.

Although the $ZnBr_2$ RFB system has a high power density that can adequately power the Jellyfish, the toxicity and corrosiveness of Br_2 is potentially problematic (*26*, *32*) (see Materials and Methods for more details). Moreover, the limited space for cathode reaction restricted the capacity of the RFB and the robot's operation time. To address these issues, we developed a ZnI_2 RFB that operates initially as a primary battery and then as a rechargeable one. Our results show that these cells can also efficiently use the energy stored in the bell's electrolyte volume and also allow rapid electrolyte exchange for physical recharging (*33*).

Primary rechargeable ZnI_2 flow battery

Figure 4A illustrates the battery configuration used for the aqueous ZnI_2 RFB with graphene and active carbon-modified electrodes, similar to the $ZnBr_2$ RFBs. Figure 4B depicts the analogous ZnI_2 RFB battery stack. Unlike $ZnBr_2$ RFBs, I_2 is safer than Br_2 making it possible to switch the flow channel of anolyte and catholyte and fully use the much larger volume of the bell. In this setup, I_2 is on the flowing catholyte side, while Zn resides on the sessile side. To establish the primary ZnI_2 RFB, we first electrodeposited 120 mA·hour cm^{-2} Zn on the graphene-coated anode and used 4 M ZnI_2 + 1 M KI + 0.3 M I_2 as catholyte. Therefore, for the first cycle, the electrochemical reactions are as follows: on the anode side, $Zn - 2e^- \rightarrow Zn^{2+}$; and on the cathode side, $I_3^- + 2e^- \rightarrow 3I^-$. In the first cycle, the cell functions as a primary battery, discharging all the stored energy in the catholyte. As shown in Fig. 4C, the primary ZnI_2 RFBs demonstrated stable operation at a current density of 20 mA cm^{-2} for up to 5 hours, exhibiting an energy density of about 11 A·hour $liter^{-1}$ and areal power density of ~110 mA·hour cm^{-2} and a discharge depth of around 69%. This discharge depth is limited by the iodine side of the battery, because as the concentration of I_3^- ions saturates, deposition occurs on the carbon felt, forming solid iodine. Solid iodine is an electrical insulator, leading to a rapid increase in overpotential and a subsequent decrease in discharge voltage. As the capacity of the electrodeposited Zn can reach up to 300 mA·hour cm^{-2}; however, there is remaining Zn left after the first round of discharge; therefore, we are able to open the valve on the bell and replace the depleted catholyte to continue operating the UUV (fig. S5). This approach for recharging robots brings advantages of its own: It introduces new modes of logistical operation compared to conventional lithium batteries.

The ZnI_2 RFB is also of interest as a rechargeable battery, albeit with a lower discharge capacity. The cycling capacity in the rechargeable operating mode was estimated as ~3 A·hour $liter^{-1}$. As illustrated in Fig. 4D, the cells also exhibited stable performance over more than 200 cycles. With a 1.2-V theoretical voltage of ZnI_2 RFB, the primary-rechargeable ZnI_2 RFB had a highest power density of ~100 mW cm^{-2} (Fig. 4E), slightly lower than that of the $ZnBr_2$ RFB system. Upon charging the ZnI_2 RFB after the primary battery cycle, the battery can operate for ~30 min in each of the subsequent cycles (Fig. 4F).

Swimming paces for the Jellyfish

The bell of the Jellyfish can store 4 liters of electrolyte solution; to make the Jellyfish swim and flow the electrolyte, we used a motor to pull on the bell. The bell chamber, molded from silicone (Smooth-On Inc.; Dragon Skin 30), has a hemispherical shape (diameter of 30 cm) that allows for more drag on the bottom than the top during

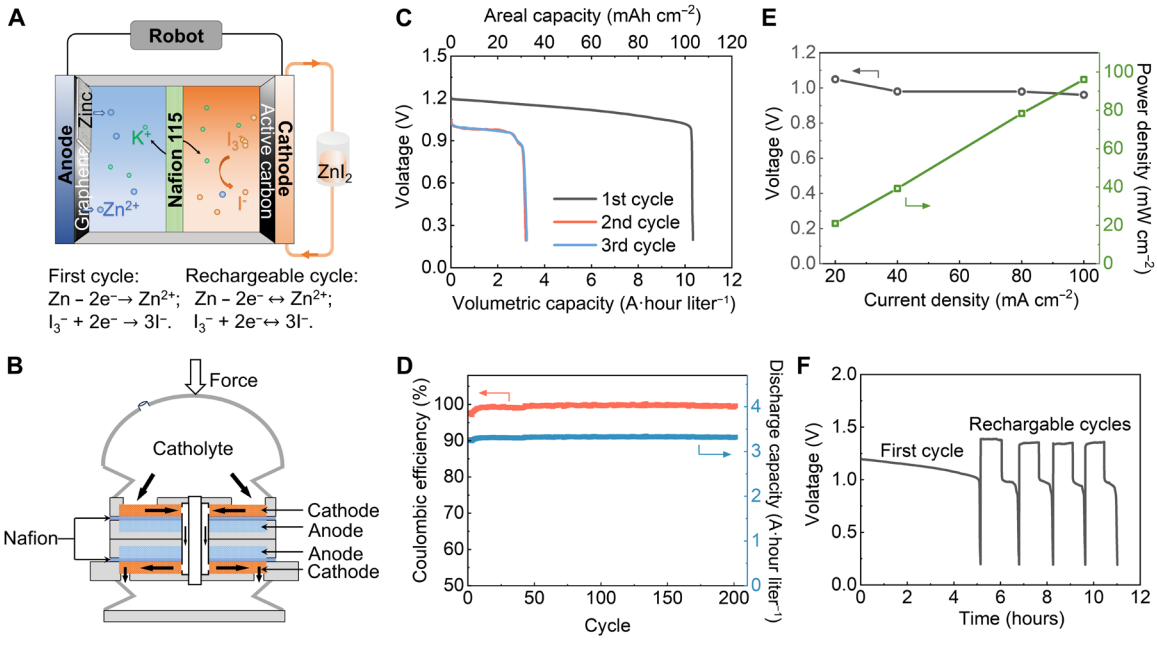

Fig. 4. Primary-rechargeable ZnI_2 flow battery system for high-capacity support of the Jellyfish. (**A**) Scheme illustrating the primary-rechargeable ZnI_2 flow battery. (**B**) The battery stack design inside the Jellyfish. (**C**) The profiles of capacity versus voltage at the first primary cycle and the following cycles at 20 mA cm^{-2}. (**D**) The cycling performance of capacity and coulombic efficiency of the flow battery after the first primary cycle at 20 mA cm^{-2}. (**E**) The voltage and power density of ZnI_2 flow battery cells at different current densities. (**F**) Galvanostatic voltage profiles of the flow battery at a current density of 20 mA cm^{-2} using 4 M ZnI_2 + 1 M KI + 0.3 M I_2.

a full stroke cycle, allowing it to swim upward. To power the motor, we assembled six $ZnBr_2$ RFBs into a stack capable of 9.6-V, 1.6-A output. We used $ZnBr_2$ solution as the catholyte at its saturation concentration of 15 M to maximize the battery's capacity. When measuring the swimming speed of the Jellyfish, we tracked the position of the bell's top, where it underwent incremental upward movements and shape alterations during the swimming process. Through this mechanism, the Jellyfish achieved an ascent speed of 2 cm s^{-1}, which cost 26.7 J to climb from the bottom of the tank to the top (Fig. 5, A and B; movies S1 and 2; and text S3). We can also see from Fig. 5A that its swimming motion matched our theoretical model, primarily determined by asymmetry in fluidic forces during different parts of the actuation cycle, as well as cyclic oscillations of its center of mass (see the Supplementary Materials for more details).

Because ZnI_2 RFB systems have a lower power density than $ZnBr_2$, we connected 10 batteries (five in series and then in parallel) to improve the robot's swimming performance. On the basis of the energy density of about 11 A·hour $liter^{-1}$ from Fig. 4C, the 4 liters of electrolyte solution gave us the total energy storage of around 44 Wh. Notably, the Jellyfish UUV solely powered by primary ZnI_2 RFBs swam for an extended duration of 1.5 hours of actual swimming time shown in movie S3. Its long swimming time is due to its 90% battery mass ratio (Fig. 6A).

In theory, this UUV has a theoretical operation time of 9 hours (see text S3 for calculations). Figure 6B depicts the progressive decline in battery limiting power from 5.1 to 3 W as molar concentration decreases, potentially accounting for the deviation from theoretical maximum operational efficiency (see text S2 and Simulation Data for simulation details). This may result from different factors, like the high concentration gradient due to the limited flow speed and reduced I_3^- amount due to solid Iodine deposition (*31*).

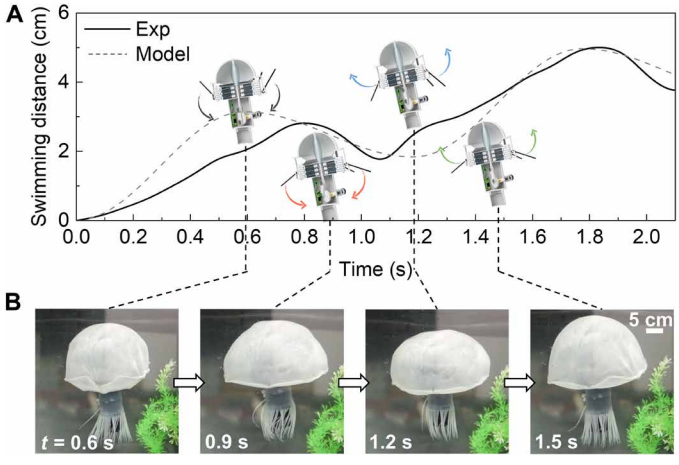

Fig. 5. Jellyfish swimming test and simulation. (**A**) Experimental and predicted swimming distance of the Jellyfish at different time with 3D model of the Jellyfish showing the robot's motion in one cycle. (**B**) Operation test corresponding to the moment in (A).

Over time, the electrolyte in the battery gradually depletes, reducing the maximal power it can supply, until it becomes insufficient to sustain the motor's functionality. Tailoring the design of the battery to simultaneously minimize the ohmic resistance, maximize the transport of electrolytes, and boost the surface area and activity of electrodes might lead to an additional increase in the operation time.

In the examined configuration, the principal source of energy consumption is the work required to transfer large volumes of fluids within the flow battery's permeable layer (required to generate mechanical movement). On the basis of our findings, the work needed to

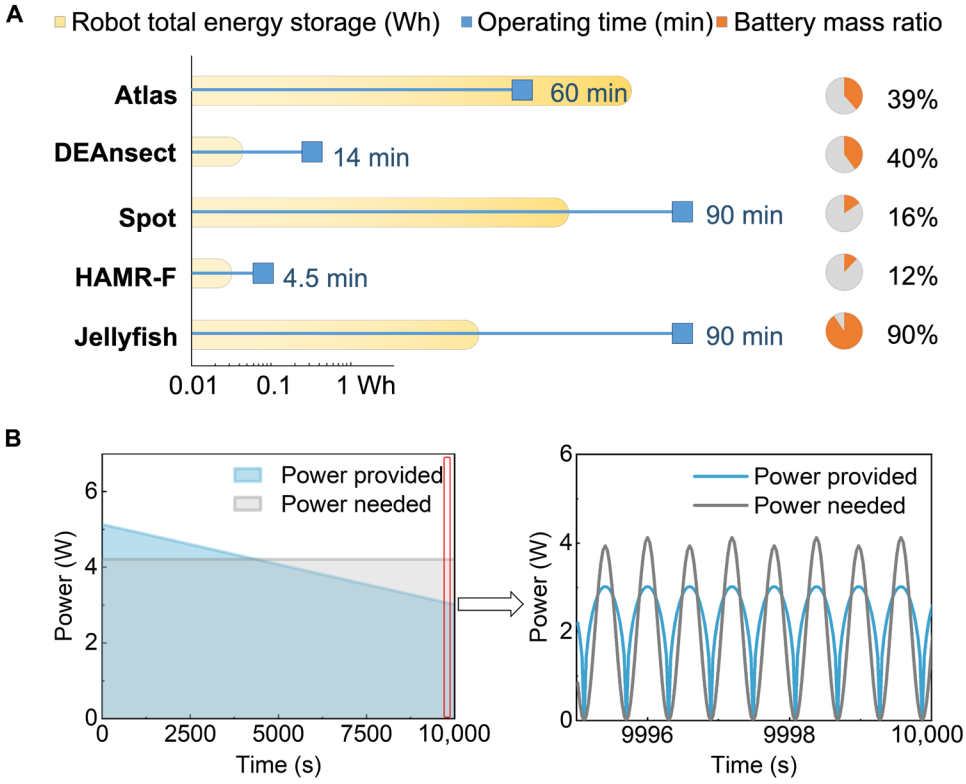

Fig. 6. Energy storage in Jellyfish and other modern robots. (**A**) Energy storage and operation time of some robotic systems. (**B**) Comparison of the predicted available power and required power for the Jellyfish operation.

overcome viscous resistance consumes ~95 to 98% of the total power produced by the motors. A future design may improve on this by allowing flow to occur also outside of the channels or, alternatively, by reducing the viscous resistance of the permeable layers. Further details on the energy efficiency of the robot can be seen in text S5.

DISCUSSION

We report that incorporation of a hydraulic power system into a robot with high volumetric (Q ~ 11 A·hour liter^{-1}) and areal (108 mA·hour cm^{-2}) energy density results in robots with long operational lifetime (T ~ 1.5 hours) and composed of primarily electrochemically energy dense liquid (~90% of the robot's weight). Our robot is the first that uses an RFB as its sole power source; it is also the first to use a rechargeable primary RFB. The motion of the electrolyte solution in the bell of the Jellyfish causes rapid ascent of the robot and, combined with its low inertia hemispherical construction, demonstrates a path to improving both the endurance and agility of robots using the embodied energy design paradigm (*20*).

The RFB chemistries studied also demonstrated high capacity and rechargeability by combining primary battery and secondary flow battery configurations (*34*). The ability to empty and refill the electrolyte in the ZnI_2 presents a simple, previously unidentified way to rapidly recharge robots and has implications in search and rescue missions, offering potentially previously unidentified modes of cooperation between machines, where wheeled or propellor-driven large robots could provide mobile bases that recharge and rapidly resupply more agile and small satellite robots.

The operational lifetime of this robot, however, falls far short of its theoretical limit. We used only 15% of the capacity of the ZnI_2 primary battery due to the decreased power density resulting from the concentration decrease during discharging (see text S3 for more details). The battery performance can be further improved by modifying electrode properties (e.g., porosity, surface area, and resistance) and optimizing the battery design (e.g., electrolyte transport and conductivity) to speed up the discharging process (see text S6 for more details).

As the robot that we present is of low inertia and of similar density to the ocean itself (ρ_{avg} ~ 0.91 g cm^{-3} without weight balance), it has immediate potential for use as a so-called Lagrangian drifter (*35*). These machines survey ocean currents and collect environmental data of ocean dynamics but, so far, have been too large and too dense to truly follow currents, particularly small ones. By passively following these currents, using the energy for sensing and infrequent ascent to communicate, these robots may provide large amounts of data for use in ocean health monitoring. Last, the cost of this robot is ~$4,300 (see text S4 for detailed cost analysis), far less than existing drifters. Therefore, many of these robots could be deployed for high density sensory networks along multiple currents.

MATERIALS AND METHODS

Robot system fabrication

In designing the Jellyfish robot system, we used Fusion 360 (Autodesk Inc.) for modeling and 3D printing. The control chamber and RFB sealings were produced on a Carbon M1 printer. The Jellyfish bell

was crafted from Dragon Skin 30 using a hemispherical mold with a 30-cm diameter. The bottom piece of the bell took the form of a ring with an inner diameter of 6 cm and an outer diameter of 30 cm, joined to the top piece using SIL-Poxy (fig. S6). We added fluorescent powder during the mixing of Dragon Skin A and B. Once cured, 5 min of exposure to UV light enabled the robot to emit a glow in the dark, as illustrated in fig. S7.

All bonding processes that did not require softness, such as bonding between the hollow SIL 30 piece and middle rod, compressible SIL 30 piece, and the RFB shell, used Loctite 405 with primer pretreatment. For sealing the RFBs, we used screws and durable O-rings to ensure electrolyte separation and avoid leaking.

RFB electrode modification

ZnI_2, KI, KCl, graphene, and active carbon were purchased from Sigma-Aldrich, and $ZnBr_2$ was purchased from Alfa Aesar. Carbon black Super-P was purchased from TIMCAL. Carbon felt was purchased from Fuel Cell Earth. The titanium mesh was from Metal Material. The Nafion 115 was purchased from DuPont.

Preparation of the electrospray ink

All electrodes used in battery and robot testing were treated by air-controlled electrospray. The anode conductive ink was graphene-dissolved in deionized (DI) water obtained from the Milli-Q water purification system. The resistivity of the DI water is 18.2 megohm cm^{-1} at room temperature. The cathode ink consisted of four primary components: AC, carbon black Super-P, 20 wt % of Nafion dispersion (Ion Power), and DI water. The Nafion dispersion acted as a binder and a suitable surfactant to mix the carbon in water. It was found that the best anode ink composition was 4 wt % of graphene and 96 wt % of DI water, while the optimized composition for cathode was 1.5 wt % of AC, 0.5 wt % of super-P, 10 wt % of Nafion dispersion, and 88 wt % of DI water. The ink was then ultrasonicated for 60 min before use to remain well dispersed.

RFB electrode modification

The ink solution was then switched to 5-ml syringes with a needle (tube gauge, 10; shell gauge, 17). Gauge of air [10 pounds $inch^{-2}$ (4.53592 kg cm^{-2})] was applied through the shell of the needle while the pump (Harvard Apparatus) pushed the syringes to spray the solution out under the voltage of 20 kV. The distance between the needle and the carbon felt was 10.5 cm. For cathode treatment, the amount of solution on the electrode was 45 μl for each spray spot and 405 μl for a single cell. The flow rate was set to 0.015 ml min^{-1}. The total amount of solution for the anode was strictly limited to, 60 μl for each spot, 360 μl for a single cell, and the flow rate was 0.02 ml min^{-1}.

RFB assembly

During our battery test, the Br_2 corroded the stainless steel mesh, our initial choice for the current collector material. Meanwhile, the high volatility of Br_2 limited our test in the flame hood and made it harder to handle in a large volume. On the basis of the result above, we decided to use Ti mesh as the current collector, which is more stable. We sealed the Br_2 in the catholyte chamber to avoid the possible release of Br_2 and make our fabrication process more handful and repeatable. The single cell used to test battery's performance comprises titanium mesh current collectors (mesh size of 0.3 mm by 0.6 mm), carbon felts, a piece of Nafion 115, and RPU 70 end plates (fig. S8). To enhance the utilization of the porous carbon felt electrode, the flow chamber, measuring 2.5 mm in thickness, is designed with a separated symmetrical polytetrafluoroethylene plastic flow frame, allowing the flowing electrolytes to flow through and effectively rinse the electrode in the same way as in the Jellyfish. To mitigate issues related to resistance and surface contact, the compressing ratio (defined as the ratio of electrode thickness prior to and post compression) is rigorously maintained at ~2 to 2.4, achieved through the strategic addition of varying quantities of gaskets.

For $ZnBr_2$ flow battery systems, the anolyte is 3 M KCl and 2 M $ZnBr_2$, and the catholyte is 15 M $ZnBr_2$ and 3 M KCl. To make sure that the volume of the tested battery is the same as that of a single battery in the robot system, we keep the analyte in the volume of 0.66 liters. To provide a flow for the anolyte similar to the robot system, we used a pump with the flow speed of 5 ml min^{-1}. On the cathode side, we used a springe to fill 10 ml of electrolyte into the chamber through a hole cover by flexshot 30 and saturated the carbon felt. Titanium mesh (mesh size of 0.3 mm by 0.6 mm) was the current collector on both sides. The effective area of the carbon felt was 40.6 cm^2 (outer diameter of 8 cm and inner diameter of 3.5 cm), while, in the primary-rechargeable ZnI_2 flow battery systems, the electrolytes are both 4 M ZnI_2 and 1 M KI, except that the catholyte has extra 0.3 M I_2 for the discharging of the first cycle. The volume of anolyte in the tested battery is 0.4 liters. In the primary battery cycle, we used an electrolytic cell to deposit zinc on the graphene-coated carbon felt with a low current of 20 mA cm^{-2} for the Zn anode side for 6 hours. In the robot test, the electrolyte concentration was the same with a total volume of 4 liters, and the motor provided the motivation for the electrolyte to flow. To refill the electrolyte after the first cycle of primary ZnI_2 flow battery, we need 4 liter/435 ml min^{-1} = 9.2 min.

The commercially available cation exchange membrane (Nafion 115, DuPont, USA) was used as the separator for the RFBs. Before assembling, the Nafion 115 membranes were treated with 5% H_2SO_4 under 100°C for 2 hours and then washed with DI water at 100°C for 1 hour.

Supplementary Materials

The PDF file includes:

Supplementary Text S1 to S6
Figs. S1 to S9
Table S1
Legend for data S1
Legends for movies S1 to S3
References

Other Supplementary Material for this manuscript includes the following:

Data S1
Movies S1 to S3

REFERENCES AND NOTES

1. G. Z. Yang, J. Bellingham, P. E. Dupont, P. Fischer, L. Floridi, R. Full, N. Jacobstein, V. Kumar, M. McNutt, R. Merrifield, B. J. Nelson, B. Scassellati, M. Taddeo, R. Taylor, M. Veloso, Z. L. Wang, R. Wood, The grand challenges of science robotics. *Sci. Robot.* **3**, eaar7650 (2018).
2. N. T. Jafferis, E. F. Helbling, M. Karpelson, R. J. Wood, Untethered flight of an insect-sized flapping-wing microscale aerial vehicle. *Nature* **570**, 491–495 (2019).
3. Z. L. Wang, Triboelectric nanogenerators as new energy technology for self-powered systems and as active mechanical and chemical sensors. *ACS Nano* **7**, 9533–9557 (2013).
4. M. Wang, D. Vecchio, C. Wang, A. Emre, X. Xiao, Z. Jiang, P. Bogdan, Y. Huang, N. A. Kotov, Biomorphic structural batteries for robotics. *Sci. Robot.* **5**, eaba1912 (2020).

5. M. T. Tolley, R. F. Shepherd, B. Mosadegh, K. C. Galloway, M. Wehner, M. Karpelson, R. J. Wood, G. M. Whitesides, A resilient, untethered soft robot. *Soft Robot.* **1**, 213–223 (2014).
6. X. Huang, K. Kumar, M. K. Jawed, A. Mohammadi Nasab, Z. Ye, W. Shan, C. Majidi, Highly dynamic shape memory alloy actuator for fast moving soft robots. *Adv. Mater. Technol.* **4**, 1800540 (2019).
7. A. D. B. L. Ferreira, P. R. O. Nóvoa, A. T. Marques, Multifunctional material systems: A state-of-the-art review. *Compos. Struct.* **151**, 3–35 (2016).
8. N. Kottege, C. Parkinson, P. Moghadam, A. Elfes, S. P. N. Singh, in *2015 IEEE International Conference on Robotics and Automation (ICRA)* (IEEE, 2015), pp. 5140–5147.
9. Z. Zhakypov, K. Mori, K. Hosoda, J. Paik, Designing minimal and scalable insect-inspired multi-locomotion millirobots. *Nature* **571**, 381–386 (2019).
10. T. Li, G. Li, Y. Liang, T. Cheng, J. Dai, X. Yang, B. Liu, Z. Zeng, Z. Huang, Y. Luo, T. Xie, W. Yang, Fast-moving soft electronic fish. *Sci. Adv.* **3**, e1602045 (2017).
11. A. J. Ijspeert, A. Crespi, D. Ryczko, J.-M. Cabelguen, From swimming to walking with a salamander robot driven by a spinal cord model. *Science* **315**, 1416–1420 (2007).
12. H. Kim, J. Choi, K. K. Kim, P. Won, S. Hong, S. H. Ko, Biomimetic chameleon soft robot with artificial crypsis and disruptive coloration skin. *Nat. Commun.* **12**, 4658 (2021).
13. G. Li, X. Chen, F. Zhou, Y. Liang, Y. Xiao, X. Cao, Z. Zhang, M. Zhang, B. Wu, S. Yin, Y. Xu, H. Fan, Z. Chen, W. Song, W. Yang, B. Pan, J. Hou, W. Zou, S. He, X. Yang, G. Mao, Z. Jia, H. Zhou, T. Li, S. Qu, Z. Xu, Z. Huang, Y. Luo, T. Xie, J. Gu, S. Zhu, W. Yang, Self-powered soft robot in the Mariana Trench. *Nature* **591**, 66–71 (2021).
14. D. Lin, Y. Liu, Y. Cui, Reviving the lithium metal anode for high-energy batteries. *Nat. Nanotechnol.* **12**, 194–206 (2017).
15. K. T. Nam, D.-W. Kim, P. J. Yoo, C.-Y. Chiang, N. Meethong, P. T. Hammond, Y.-M. Chiang, A. M. Belcher, Virus-enabled synthesis and assembly of nanowires for lithium ion battery electrodes. *Science* **312**, 885–888 (2006).
16. M. Wehner, R. L. Truby, D. J. Fitzgerald, B. Mosadegh, G. M. Whitesides, J. A. Lewis, R. J. Wood, An integrated design and fabrication strategy for entirely soft, autonomous robots. *Nature* **536**, 451–455 (2016).
17. C. A. Aubin, S. Choudhury, R. Jerch, L. A. Archer, J. H. Pikul, R. F. Shepherd, Electrolytic vascular systems for energy-dense robots. *Nature* **571**, 51–57 (2019).
18. X. Yang, L. Chang, N. O. Perez-Arancibia, An 88-milligram insect-scale autonomous crawling robot driven by a catalytic artificial muscle. *Sci. Robot.* **5**, eaba0015 (2020).
19. C. A. Aubin, R. H. Heisser, O. Peretz, J. Timko, J. Lo, E. F. Helbling, S. Sobhani, A. D. Gat, R. F. Shepherd, Powerful, soft combustion actuators for insect-scale robots. *Science* **381**, 1212–1217 (2023).
20. C. A. Aubin, B. Gorissen, E. Milana, P. R. Buskohl, N. Lazarus, G. A. Slipher, C. Keplinger, J. Bongard, F. Iida, J. A. Lewis, R. F. Shepherd, Towards enduring autonomous robots via embodied energy. *Nature* **602**, 393–402 (2022).
21. R. A. Watson, S. G. Ficici, J. B. Pollack, Embodied evolution: Distributing an evolutionary algorithm in a population of robots. *Robot. Auton. Syst.* **39**, 1–18 (2002).
22. W. M. Megill, J. M. Gosline, R. W. Blake, The modulus of elasticity of fibrillin-containing elastic fibres in the mesoglea of the hydromedusa *Polyorchis penicillatus*. *J. Exp. Biol.* **208**, 3819–3834 (2005).
23. Y. Yao, J. Lei, Y. Shi, F. Ai, Y.-C. Lu, Assessment methods and performance metrics for redox flow batteries. *Nat. Energy* **6**, 582–588 (2021).
24. D. Chao, W. Zhou, F. Xie, C. Ye, H. Li, M. Jaroniec, S.-Z. Qiao, Roadmap for advanced aqueous batteries: From design of materials to applications. *Sci. Adv.* **6**, eaba4098 (2020).
25. S. Jin, J. Yin, X. Gao, A. Sharma, P. Chen, S. Hong, Q. Zhao, J. Zheng, Y. Deng, Y. L. Joo, L. A. Archer, Production of fast-charge Zn-based aqueous batteries via interfacial adsorption of ion-oligomer complexes. *Nat. Commun.* **13**, 2283 (2022).
26. B. Li, Z. Nie, M. Vijayakumar, G. Li, J. Liu, V. Sprenkle, W. Wang, Ambipolar zinc-polyiodide electrolyte for a high-energy density aqueous redox flow battery. *Nat. Commun.* **6**, 6303 (2015).
27. R. V. Adith, R. P. Naresh, K. Mariyappan, M. Ulaganathan, P. Ragupathy, An optimistic approach on flow rate and supporting electrolyte for enhancing the performance characteristics of Zn-Br2 redox flow battery. *Electrochim. Acta* **388**, 138451 (2021).
28. Z. Pei, Z. Zhu, D. Sun, J. Cai, A. Mosallanezhad, M. Chen, G. Wang, Review of the $I^-/I3^-$ redox chemistry in Zn-iodine redox flow batteries. *Mater. Res. Bull.* **141**, 111347 (2021).
29. J. Zheng, Q. Zhao, T. Tang, J. Yin, C. D. Quilty, G. D. Renderos, X. Liu, Y. Deng, L. Wang, D. C. Bock, C. Jaye, D. Zhang, E. S. Takeuchi, K. J. Takeuchi, A. C. Marschilok, L. A. Archer, Reversible epitaxial electrodeposition of metals in battery anodes. *Science* **366**, 645–648 (2019).
30. J. Zheng, L. A. Archer, Crystallographically textured electrodes for rechargeable batteries: Symmetry, fabrication, and characterization. *Chem. Rev.* **122**, 14440–14470 (2022).
31. S. Jin, Y. Shao, X. Gao, P. Chen, J. Zheng, S. Hong, J. Yin, Y. L. Joo, L. A. Archer, Designing interphases for practical aqueous zinc flow batteries with high power density and high areal capacity. *Sci. Adv.* **8**, eabq4456 (2022).
32. P. Bai, M. Z. Bazant, Performance and degradation of a lithium-bromine rechargeable fuel cell using highly concentrated catholytes. *Electrochim. Acta* **202**, 216–223 (2016).
33. V. Viswanathan, A. H. Epstein, Y.-M. Chiang, E. Takeuchi, M. Bradley, J. Langford, M. Winter, The challenges and opportunities of battery-powered flight. *Nature* **601**, 519–525 (2022).
34. Y. Li, L. Li, Y. Zhao, C. Deng, Z. Yi, D. Xiao, N. Mubarak, M. Xu, J. Li, G. Luo, Q. Chen, J. K. Kim, Homogenizing zn deposition in hierarchical nanoporous cu for a high-current, high areal-capacity Zn flow battery. *Small* **19**, e2303005 (2023).
35. S. Subbaraya, A. Breitenmoser, A. Molchanov, J. Muller, C. Oberg, D. A. Caron, G. S. Sukhatme, Circling the seas: Design of lagrangian drifters for ocean monitoring. *IEEE Robot. Autom. Mag.* **23**, 42–53 (2016).
36. P. Wegener, *What makes airplanes fly?: History, Science, and Applications of Aerodynamics* (Springer Science & Business Media, 1997).
37. J. Bear, M. Y. Corapcioglu, eds., *Fundamentals of Transport Phenomena in Porous Media* (Springer Science & Business Media, 2012), vol. 82.
38. A. Tang, B. Jie, M. Skyllas-Kazacos, Studies on pressure losses and flow rate optimization in vanadium redox flow battery. *J. Power Sources* **248**, 154–162 (2014).
39. D. Schmal, J. Van Erkel, P. J. Van Duin, Mass transfer at carbon fibre electrodes. *J. Appl. Electrochem.* **16**, 422–430 (1986).
40. X. Ma, H. Zhang, F. Xing, A three-dimensional model for negative half cell of the vanadium redox flow battery. *Electrochim. Acta* **58**, 238–246 (2011).

Acknowledgments

Funding: This work was supported by the Office of Naval Research, contracts N00014-20-1-2438 and N00014-22-1-2595. L.A.A. also acknowledges support from the Department of Energy Basic Energy Sciences Program through award DE-SC0016082 for developing the zinc anode designs used in the study. **Author contributions:** R.F.S. and L.A.A. conceived the idea of the study and supervised the project. X.L. and S.J. planned experiments. X.L., S.J., and Y.S. carried out experiments and researched, collected, and analyzed data. S.K. and A.D.G. conducted simulations. X.L. and S.J. drafted the initial manuscript. All authors discussed the results and contributed to the final manuscript. **Competing interests:** The authors declare that they have no competing interests. **Data and materials availability:** All data needed to evaluate the conclusions in the paper are present in the paper and/or the Supplementary Materials.

Submitted 29 May 2024
Accepted 24 October 2024
Published 27 November 2024
10.1126/sciadv.adq7430